

TRACING THE SPIRAL STRUCTURE OF THE OUTER MILKY WAY WITH DENSE ATOMIC HYDROGEN GAS

BON-CHUL KOO, GEUMSOOK PARK, WOONG-TAE KIM, AND MYUNG GYOON LEE
Department of Physics and Astronomy, Seoul National University
Seoul 151-747, Korea

DANA S. BALSER
National Radio Astronomy Observatory,
520 Edgemont Road, Charlottesville VA 22903-2475, USA

TREY V. WENGER
Astronomy Department, University of Virginia,
P.O. Box 400325, Charlottesville, VA, 22904-4325, USA
and
National Radio Astronomy Observatory,
520 Edgemont Road, Charlottesville VA 22903-2475, USA

ABSTRACT

We present a new face-on map of dense neutral atomic hydrogen (HI) gas in the outer Galaxy. Our map has been produced from the Leiden/Argentine/Bonn (LAB) HI 21-cm line all-sky survey by finding intensity maxima along every line of sight and then by projecting them on the Galactic plane. The resulting face-on map strikingly reveals the complex spiral structure beyond the solar circle, which is characterized by a mixture of distinct long arcs of HI concentrations and numerous ‘interarm’ features. The comparison with more conventional spiral tracers confirms the nature of those long arc structures as spiral arms. Our map shows that the HI spiral structure in the outer Galaxy is well described by a four-arm spiral model (pitch angle of 12°) with some deviations, and gives a new insight into identifying HI features associated with individual arms.

Keywords: Galaxy: structure – ISM: structure – radio lines: ISM

1. INTRODUCTION

Spiral arms are sites of active star formation with dense interstellar material, so that young stars, star-forming regions, HII regions, and molecular clouds are their conventional tracers. In the outer Galaxy, where star-formation activity is low, such ‘strong’ tracers are sparse and neutral atomic hydrogen (HI) gas is a useful tracer: the 21-cm emission line emitted from the transition between the two hyperfine levels of the HI atom can be used to trace spiral arms that have a higher density of HI gas than the Galactic average.

A conventional approach to explore the HI spiral structure is to produce a face-on map of the Galaxy from large-scale HI 21-cm line surveys. One can transform the observed line flux in a given narrow velocity interval along the line of sight to the HI column density in the corresponding distance interval. By doing this for every Galactic longitude (l) and latitude (b) and by projecting the resulting data cube along the direction perpendicular to the Galactic plane, one can obtain a face-on map of the Galactic HI distribution (e.g., [Burton 1974](#); [Binney & Merrifield 1998](#)). The main difficulty in this kinetic approach lies in transforming the Local-Standard-of-Rest (LSR) velocity (v_{LSR}) to the Galactocentric distance, which is usually alleviated by assuming a circular rotation. Aside from the uncertainty in the adopted Galactic rotation curve, the non-circular motions due to streaming along the spiral arms and the ‘velocity crowding’ can seriously distort the HI structure in real space (e.g., [Burton 1971](#)). This is particularly problematic for the inner Galaxy where the line of sight crosses tangential points and an ambiguity in distance occurs for a given LSR velocity. Harold Weaver, for example, suggested that the longitude-velocity (l, v_{LSR}) diagram should be considered

as the proper end product (Simonson 1970), which may be compared with dynamical models. For the outer Galaxy, however, these problems are less serious except near $l = 0^\circ$ and 180° where the velocity varies little with heliocentric distance, and the HI face-on map can reliably show the spiral structure with some caveats if we can separate out dense HI gas associated with spiral arms.

The first HI face-on maps of the outer Galaxy appeared in the 1950s (van de Hulst et al. 1954; Westerhout 1957; Oort et al. 1958), which were soon followed by other maps suggesting different interpretations (Kerr 1969; Weaver 1970; Verschuur 1973; Weaver 1974). In order to show the spiral structure, they produced face-on maps either by projecting maximum densities in the z -direction, i.e., in the direction perpendicular to the plane, on the Galactic plane (Westerhout 1957; Oort et al. 1958) or by transforming the loci of HI 21-cm line peaks into real space and by connecting them (Kerr 1969; Weaver 1970; Verschuur 1973; Weaver 1974). In his review paper, Simonson (1970) showed that the two most up-to-date maps at that time, i.e., the maps by Kerr (1969) and Weaver (1970), agree with each other except a few points. As we will see in later in § 2, the sketch by Kerr (1969) indeed accurately shows the ridges of dense HI concentrations. But without demonstrating the association of more conventional spiral tracers, the identity of these features as spiral arms could have not been verified. After these initial works, the efforts to explore the global spiral structure of the outer Galaxy using HI face-on maps have been rather scarce. As far as we are aware, until 2005, the only published HI face-on maps showing the entire outer Galactic plane were those in Henderson et al. (1982) and Nakanishi & Sofue (2003). Their surface density maps clearly showed three spiral arms; the Perseus and Outer (or Norma-Cygnus) arms in the northern Galaxy ($l = 0^\circ$ – 180°) and the Sagittarius-Carina (hereafter Sgr-Car) arm in the southern Galaxy ($l = 180^\circ$ – 360°).¹

More recently, as the sensitive HI data of half-degree resolution from the LAB all-sky survey became available (Kalberla et al. 2005; Hartmann & Burton 1997; Bajaja et al. 2005; Arnal et al. 2000), new face-on maps of the outer Galaxy have been published (Levine et al. 2006a; Nakanishi & Sofue 2016). These new face-on maps of total HI surface density showed the above three spiral arm structures better than the earlier maps and revealed another arm structure in the southern Galaxy. But in regions where the Galactic plane is thick and severely warped and flared, i.e., the far side of the northern Galaxy, the maps were rather smooth without any hint of an arm-like structure. Levine et al. (2006a) applied an unsharp masking technique which showed the spiral arm features more clearly, but it did not reveal new major spiral structures other than the ones that can be inferred from the total surface density map. They noted that, in several places, the distribution of over-dense regions in their perturbed surface density map deviates from the spiral model based on HII regions (Georgelin & Georgelin 1976; Wainscoat et al. 1992), which has four spiral arms with pitch angles of 12° – 13° . Instead, a fit to their perturbed surface density map resulted in HI “spiral arms” with significantly larger pitch angles of 21° – 25° .

In this paper, we present a new HI face-on map of the outer Galaxy and re-examine the HI global spiral structure. Our map has also been produced from the LAB survey data but by employing a method similar to those used in early studies; we first find local density maxima along sight lines and then add up their mass density along the z axis (§ 2). This face-on map of dense HI concentrations gives a striking view of the complex spiral structure beyond the solar circle, characterized by a mixture of distinct long arcs and numerous interarm features. As we will show in § 3, the known conventional spiral tracers are found to be concentrated along the HI ridges, which verifies the identity of long arc structures as spiral arms. We will further show that the global HI spiral structure in the outer Galaxy connects smoothly to the massive star-forming regions in the inner Galaxy and that they are described well by a four-arm spiral model (pitch angle 12°) with some deviations. We will also discuss HI features associated with individual arms in § 3.

2. DATA AND FACE-ON MAP PRODUCTION

We use the LAB HI 21-cm line survey data. The survey combined three independent surveys of angular resolution of $30'$ – $36'$ to produce all-sky data at 0.5 pixels with an rms noise of 0.07 – 0.09 K in brightness temperature. We first determine the local maxima in each line profile. We use the IDL procedure PEAKFINDER², developed by Christophe Morisset (UNAM, Mexico). The code finds local maxima from their derivatives and then determines the significance of a peak from its width and weight. The width of a peak is the number of data points that have positive derivative at its left plus the number of data points with negative derivative at its right, and the weight is the sum of the absolute values of the derivatives inside the width. We adopted the peaks with the weights ≥ 0.5 and $T_b > 0.5$ K, which adequately identifies all distinct intensity maxima in the spectra (Figure 1).

¹ The terms “southern Galaxy” and “northern Galaxy” are used to represent the Galactic areas that are mainly visible from the southern and northern hemispheres, respectively.

² The code can be obtained at http://132.248.1.102/~morisset/idl_cours/IDL/index_local.htm.

The (l, b, v_{LSR}) cube of the local maxima brightness temperature, $T_{b,\text{max}}(l, b, v_{\text{LSR}})$, is used to fill up the three-dimensional spatial data cube of the H I mass density $\rho_{\text{H}}(x, y, z)$. We first determine (l, b, v_{LSR}) of each (x, y, z) pixel and obtain its T_b from a trilinear interpolation using the IDL routine INTERPOLATE. The conversion from (x, y, z) to v_{LSR} is carried out by using a flat rotation curve with the distance to the Galactic center $R_0 = 8.34$ kpc and the rotational speed of the Sun $\Theta_0 = 240$ km s $^{-1}$, which has been suggested from the parallax-based distances and proper motions of high massive star forming regions (HMSFRs) (Reid et al. 2014; Reid & Dame 2016b). The Sun’s rotation speed is considerably greater than the IAU value (220 km s $^{-1}$), and the authors attributed the difference to the biased estimate of Θ_0 from the H I data due to the curvature in the rotation curve (Reid & Dame 2016b). From $T_b(x, y, z)$, the H column density per unit velocity ΔN_{H} is obtained at every voxel and it is converted to the H I mass density $\rho_{\text{H}}(x, y, z)$ dividing by $|dr/dv_{\text{LSR}}|$, i.e.,

$$\frac{\rho_{\text{H}}(x, y, z)}{m_{\text{H}}} = \frac{\Delta N_{\text{H}}(x, y, z)}{|dr/dv_{\text{LSR}}|} = 0.591 \frac{T_b(x, y, z)}{|dr/dv_{\text{LSR}}|} \frac{\tau_{\nu}}{1 - e^{-\tau_{\nu}}} \text{ cm}^{-3}, \quad (1)$$

where in the second equation, τ_{ν} is the 21-cm optical depth and T_b and $|dr/dv_{\text{LSR}}|$ are in units of K and pc (km s $^{-1}$) $^{-1}$, respectively. The optical depth has been estimated by assuming a constant spin temperature 155 K (see, for example, Levine et al. 2006b, for details). We emphasize that, since we sample only T_b at intensity maxima in the spectra, the resulting data cube $\rho_{\text{H}}(x, y, z)$ represents a very limited mass/volume of dense H I gas, and the column density projected to the Galactic plane will be much less than the total H I column density of the Galactic disk. But as far as the intensity peaks are due to H I concentrations, the resulting face-on map should be a representative map of dense H I gas.

Our spatial data cube covers an area of 50×50 kpc 2 in the plane and ± 6 kpc in the direction perpendicular to the plane. This z -range covers most of the warped Galactic plane: the height of the northern Galactic plane above the $b = 0^\circ$ plane increases almost linearly with Galactocentric distance and reaches +4 kpc at $R = 22$ kpc at $l = 90^\circ$, while that of the southern Galactic plane increases with R , reaching 1 kpc (at $l = 270^\circ$) below the $b = 0^\circ$ plane at 16 kpc, and then decreases back to the $b = 0^\circ$ plane (Burton 1988; Levine et al. 2006b). The voxel size of the spatial cube is 50 pc. The angular resolution ($30'$) of the LAB survey corresponds to 42 pc at 5 kpc and 170 pc at a distance of 20 kpc, so that the cube undersamples the area near the Sun but oversamples the area on the opposite side of the Galactic center (see Levine et al. 2006a). The two-dimensional map of the H I mass surface density ($\Sigma_{\text{HI}}(x, y)$) in this paper is obtained by summing the above three-dimensional cube along the direction perpendicular to the plane from -3 to $+6$ kpc and then smoothing by a Gaussian kernel with FWHM of 500 pc.

The adopted rotation curve has a small effect on the resulting face-on map. If we use the flat rotation curve with $R_{\odot} = 8.5$ kpc and $\Theta_0 = 220$ km s $^{-1}$, all the H I features slightly shift away from the Galactic center but their morphology remains the same. On the other hand, if we use the rotation curve recently proposed to correct the large H I surface density contrast across the Sun-Galactic center line (Levine et al. 2006b), the curvature of H I features slightly changes near galactic longitudes $l = 0^\circ$ and 180° , where an epicyclic streaming motion correction has been made. Since we will be comparing the H I spiral structures to the distribution of HMSFRs in the inner Galaxy, we use the rotation curve based on the HMSFR data (Reid et al. 2014; Reid & Dame 2016b).

3. RESULTS AND DISCUSSION

3.1. H I Face-on Map of the Outer Galaxy

Figure 2 is our H I face-on map of the outer Galaxy, which strikingly shows the complex spiral structure of the H I concentrations in the outer Galaxy. We see several prominent long ($\gtrsim 20$ kpc) arcs that might be segments of major spiral arms. There are also numerous ridges either connecting these spiral arm features or branching out from them. In Figure 3 (a)-(b), we compare our map with the sketches of H I spiral structure by Kerr (1969) and Weaver (1970) (Simonson 1970). It is clear that these sketches of early H I studies properly showed the locations and shapes of the major features. Some of the Kerr’s ridges are slightly shifted from the bright features in our map, which might be due to the different data sets used in the two studies. We also compare our map with the face-on map of perturbed surface densities obtained by Levine et al. (2006a) in Figure 3 (c)-(d). Note that the Levine’s map was obtained by processing the total surface density map so that it shows the areas of excess *surface densities*, while our map is obtained by processing the data cube *before* integrating along the z -axis and it shows dense regions traced by intensity peaks. The appearances of the two maps are quite different, although the locations of prominent features agree in general. Our map shows the continuous arm structures more clearly in great detail and also reveals new features. In the far side of the northern Galaxy where the Galactic plane is severely warped and flared, for example, there is a distinct thin and long arc structure at $(l, R) = (15^\circ, 12 \text{ kpc})$ to $(70^\circ, 16 \text{ kpc})$ in our map, but no coherent arm feature is apparent

in the map of [Levine et al. \(2006a\)](#). This structure is a segment of the outer Scutum-Centaurus (hereafter Sct-Cen) arm ([Dame & Thaddeus 2011](#), see below), and it demonstrates the advantage of our technique in tracing the spiral structure.

The identity of the H I arc structures in [Figure 2](#) as spiral arms can be confirmed by comparing to the distribution of other more conventional spiral tracers. In [Figure 4](#) (top panel), we overlay the distribution of H II regions and CO clouds on the H I face-on map. The distances to these sources are derived in the same way as the H I concentrations in order to avoid an offset due to the uncertainties in converting observed LSR velocities to Galactocentric distances. The red crosses represent the H II regions in the outer Galaxy from the catalog of the all-sky *Wide-Field Infrared Survey Explorer* (*WISE*) survey ([Anderson et al. 2014](#)), while the other symbols mark CO molecular clouds detected in the outer Galaxy ([May et al. 1997](#); [Vázquez et al. 2008](#); [Dame & Thaddeus 2011](#); [Sun et al. 2015](#); [Du et al. 2016](#)). Only the area between $l = 100^\circ$ and 150° has been fully mapped in CO emission at sufficient angular resolution ($\sim 1'$) ([Sun et al. 2015](#); [Du et al. 2016](#)). We will discuss the association of these sources with individual H I spiral-arm features in the following section, but their association with the H I filamentary structures is clear in [Figure 4](#). For example, we see strong concentration of H II regions along the H I arc structure at $(285^\circ, 8.3 \text{ kpc})$ to $(320^\circ, 10 \text{ kpc})$ which is the well-known Sgr-Car arm, while the clustered H II regions between $l = 105^\circ$ and 155° at $R = 10\text{--}12 \text{ kpc}$ represent a segment of the Perseus arm. The concentrated H II regions along the solar circle near the Sun belong to the Local arm which has been known as a minor spiral arm but with star formation rate comparable to those of major spiral arms ([Xu et al. 2016](#)). The H I structure associated with the Local arm is not particularly apparent in our map. [Figure 4](#) also shows that some interarm H I structures have associated H II regions indicating massive star formation in these structures, e.g., see the $\sim 4 \text{ kpc}$ -long ridge from $(40^\circ, 14 \text{ kpc})$ to $(48^\circ, 12 \text{ kpc})$. Similar figures comparing the distribution of spiral-arm tracers with the H I map of [Nakanishi & Sofue \(2003\)](#) or that of [Levine et al. \(2006a\)](#) may be found in other works ([Efremov 2011](#); [Hou & Han 2014](#)). We should also mention that the association of H I structures with CO clouds has been explored in the above mentioned CO works ([Dame & Thaddeus 2011](#); [Sun et al. 2015](#); [Du et al. 2016](#)).

There are caveats for [Figure 2](#). First, some spiral arm segments could have been shifted and/or deformed by non-circular motions. Spiral arms with strength similar to those in the Milky way are known to excite non-circular streaming motions of order $10\text{--}20 \text{ km s}^{-1}$ (e.g., [Fresneau et al. 2005](#); [Kim & Kim 2014](#); [Erroz-Ferrer et al. 2015](#)), which can shift their locations in real space by a few kpc during the mapping. It is difficult to locate such shifts or deformations in [Figure 2](#) without prior information. We mention some known features in the next section. Second, there are artifacts around the solar circle ($R = 8.34 \text{ kpc}$) due to the H I gas in the solar neighborhood, i.e., the local H I gas at $v_{\text{LSR}} \neq 0 \text{ km s}^{-1}$ is mapped to the other side of the solar circle in the real space. Such artifacts can be identified by looking at [Figure 4](#) (bottom frame), which shows the mass-weighted mean height, $\langle z \rangle \equiv \int z \rho(z) dz / \Sigma_{\text{HI}}$, of the H I concentrations. We can see that, for example, the strong emission from $l \approx 300^\circ$ to 345° just outside the solar circle has a very large scale height, which indicates that it is mostly due to local gas having a small positive v_{LSR} . Third, the surface density in [Figure 2](#) is a fraction of total H I surface density. It represents the projected surface density of dense H I gas *at intensity peaks*, averaged over $\sim 500 \text{ pc}$ (see § 2). The comparison to the total surface density map, which may be found in [Levine et al. \(2006a\)](#) or [Nakanishi & Sofue \(2016\)](#) and is not shown here, indicates that the surface density in [Figure 2](#) is $\lesssim 10\%$ of the total surface density. Before the smoothing, the surface density within a pixel (50 pc) is as large as 30% of the total surface density. [Figure 2](#) shows the relative brightnesses of H I structures, but it should not be used for a quantitative comparison with other spiral tracers, e.g., CO intensity.

3.2. H I *Spiral Arms and the Four-arm Spiral Model*

[Figure 2](#) makes it clear that the H I concentrations in the outer Galaxy have complex spiral features but with enough regularity suggesting a global spiral pattern. We compare the H I distribution to the four-arm spiral model with a constant pitch angle along each arm (see [Georgelin & Georgelin 1976](#); [Wainscoat et al. 1992](#); [Churchwell et al. 2009](#); [Efremov 2011](#); [Vallée 2014, 2015](#); [Bobylev & Bajkova 2014](#); [Hou & Han 2014](#)). In this model, the spiral pattern has four, roughly equally-spaced, major arms, i.e., the Sgr-Car, Perseus, Outer, and Sct-Cen arms, with a mean global pitch angle between 12 and 14 deg .² It has been shown that some H I arc structures are well described by this global model ([Levine et al. 2006a](#); [Nakanishi & Sofue 2016](#), and references therein). On the other hand, observations of external galaxies indicate that the pitch angle can vary considerably along individual arms ([Savchenko & Reshetnikov 2013](#); [Davis & Hayes 2014](#); [Honig & Reid 2015](#), and references therein). In the Milky Way, trigonometric parallax

² The spiral arms are referred to by different names, e.g., the Norma-Cygnus arm for the Outer arm, and the Scutum-Crux arm for the Scutum-Centaurus arm ([Vallée 2014](#)).

measurements of HMSFRs also found a considerable variation of pitch angles (7° – 20°) among 5–10 kpc segments of spiral arms (Reid et al. 2014, 2016a, and references therein). Our H I face-on map also shows such variations of pitch angles along some long ridges, but here we will be focusing on the global spiral structure. In Figure 5 (top frame), we plot the distribution of the HMSFR with accurate distances (Reid et al. 2016a) on our H I map. Recall that the kinematic distances to the H I concentrations have been computed by using the rotation curve obtained from the HMSFR data (Reid et al. 2014), so that it is justified to compare these two different category sources, i.e., H I concentrations and HMSFRs. We find that the two well-established H I spiral arm features, i.e., the Sgr-Car arm in the southern Galaxy and the outer Sct-Cen arm in the northern Galaxy (see below), can be well connected to the HMSFRs in the inner Galaxy by logarithmic spirals over 180° and 360° in Galactocentric azimuth, respectively. For the other two arms, i.e., the Perseus and the Outer arms, there is currently considerable confusion in the identification of their associated H I features as we will discuss below, but in our map we can clearly identify H I long arcs matching these arms in the four-arm spiral model.

In order to facilitate discussion and also for quantitative analysis, we need traces of H I ridges giving the positions of H I arm structures. This has been done in an (l, v_{LSR}) diagram where we can see the structures even around $l = 0^\circ$ and 180° , and the procedure is explained in the Appendix. Here we give a brief summary. We first obtained a two-dimensional (l, v_{LSR}) map by integrating the three dimensional cube of local peak intensities, $T_{b,\text{max}}(l, b, v_{\text{LSR}})$, along the b axis and determined the traces of all H I ridges by delineating the H I peak positions in an unbiased way. We then choose the ridges/traces that are thought to be the segments of major arms. For the well-established arm features or for the coherent long arc structures, this procedure is rather straightforward. But in the areas with complicated structures, e.g., between $l = 100^\circ$ and 150° , or for the features of confusing identity (see below), this procedure is subjective. It is, however, clear that two- or three-arm models cannot describe the regularity of the observed H I spiral structure, and the selected ridges are allocated to one of the four spiral arms. The locations of adopted ridges in the (l, v_{LSR}) diagram and their arm identification are summarized in Table A1. Similar spiral-arm traces had been obtained by Weaver (1974) and Reid et al. (2016a), and we compare ours to those of Reid et al. (2016a) in the Appendix. They agree with each other for most arm features, but some ridges are assigned to different spiral arms (see below). The selected spiral arm traces in the (l, v_{LSR}) diagram are then mapped to the real space, which are shown as dotted lines in Figure 5 (bottom frame). Note that we selected two ridges for some portions of spiral arms when there are two parallel branches or when the arms bifurcate at their ends. We emphasize that these traces are mainly to facilitate the discussion. In the quantitative analysis below, only the well-established traces of the Sgr-Car and the Sct-Cen arms are used.

We can now derive the parameters of the Sgr-Car and Sct-Cen spiral arms that have well-established H I features. As we mentioned in § 3.1, the thin and long arc structure at $(l, R) = (15^\circ, 12 \text{ kpc})$ to $(70^\circ, 16 \text{ kpc})$ in Figure 5 is the segment of the outer Sct-Cen arm (Dame & Thaddeus 2011) and, together with the HMSFRs in the inner Galaxy, it delineates the Sct-Cen arm over 360° in Galactocentric azimuth ϕ . Figure 6 is a plot of $\log R$ versus ϕ for all spiral tracers, clearly showing that the Sct-Cen arm can be modeled as a logarithmic spiral with a well-defined pitch angle. We fit the distribution of the HMSFRs and the H I trace by $\log(R(\phi)/R_0) = (\phi - \phi_0) \tan \psi$, where $\phi = \phi_0$ at $R = R_0$ and ψ is the arm pitch angle, that is, the angle between the tangents of the spiral arm and the circle at that point. The weights are given to the H I traces so that their total weight is equal to that of the HMSFRs, but the result does not depend on the details of the weighting. The least-squares fit to $\log R$ versus ϕ yields $\psi = 12^\circ.4 \pm 1^\circ.8$ and $\phi_0 = 288^\circ \pm 47^\circ$. The derived pitch angle is consistent with the mean global pitch angle obtained in previous studies, i.e., $\sim 12^\circ$ (Vallée 2014). The Sgr-Car arm also has a well-known H I feature which extends from $(285^\circ, 8.3 \text{ kpc})$ to $(320^\circ, 10 \text{ kpc})$ in Figure 5. If we do the same analysis for the Sgr-Car arm, we obtain $\psi = 10^\circ.9 \pm 2^\circ.8$ and $\phi_0 = 225^\circ \pm 58^\circ$. But considering the small ($\sim 180^\circ$) coverage in ϕ and the large error bar, we may instead adopt the same pitch angle ($12^\circ.4$) assuming symmetric arms and fit only ϕ_0 . In this case, we obtain $\phi_0 = 223^\circ \pm 17^\circ$, and the spacing between the Sgr-Car and Sct-Cen arms at the solar circle is 9.5 kpc. For the other two arms, i.e., the Perseus and Outer arms, their identification is controversial (see below). So we just draw spirals in Figure 5 obtained by rotating the above two spirals by 180° in ϕ , i.e., $\phi_0 = 108^\circ$ and 43° with the same pitch angle ($12^\circ.4$) for the Perseus and Outer arms, respectively, to facilitate the discussion. The parameters of the spiral arms in Figure 5 are summarized in Table 1. In the following we briefly discuss individual major arm features:

(1) Sgr-Car arm

The Sgr-Car arm appears as a coherent, narrow structure extending over 20 kpc from $l = 285^\circ$ to 345° . This H I structure as well as its association with H II regions has been well established (e.g., Georgelin & Georgelin 1976; Hou & Han 2014). Figure 5 shows that there are several faint interarm ridges connecting to the Perseus arm between

$l = 305^\circ$ and 330° . The long ridge from $(318^\circ, 12 \text{ kpc})$ to $(330^\circ, 16 \text{ kpc})$ is noticeable. The H I structure connects well to the HMSFRs in the inner Galaxy by a logarithmic spiral with a pitch angle of $12^\circ.4$, considerably greater than $6^\circ.9$ obtained from the HMSFRs in the inner Galaxy alone (Reid et al. 2014).

(2) Perseus arm

In the northern Galaxy, the Perseus arm in H I appears to be composed of several short segments between $l = 60^\circ$ and 155° . This section of the Perseus arm has been well known (Georgelin & Georgelin 1976), but its location and shape are uncertain due to non-circular motions. At $l = 110^\circ\text{--}155^\circ$, the Perseus arm sources have peculiar velocities of $10\text{--}20 \text{ km s}^{-1}$, so that their locations are considerably ($\sim 2 \text{ kpc}$) shifted outwards (Xu et al. 2006; Reid et al. 2014). This can be seen in Figure 5 where the locations of HMSFRs expected from their LSR velocities are marked by thin solid lines stretching out from their symbols. There is an H I arc structure that extends from $l = 90^\circ\text{--}110^\circ$ at $R = 11.5 \text{ kpc}$ and is overlapped with many H II regions. The structure has $v_{\text{LSR}} = -70 \text{ km s}^{-1}$ to -60 km s^{-1} and could be an interarm structure (see the Appendix). Zhang et al. (2013) and Reid et al. (2016a) pointed out a dearth of HMSFRs in the Perseus arm between $l = 50^\circ$ and 80° . Figure 4 also shows a clumpy distribution of WISE H II regions with gaps in this longitude range (see also Figure 5 of Reid et al. 2016a). The H I concentrations fill in these gaps and provide complementary information for tracing spiral arms. The model spiral arm opposite to the Sct-Cen arm with the same ($12^\circ.4$) pitch angle can describe this section of the Perseus arm reasonably well (Figure 5).

In the southern Galaxy, the identification of the Perseus arm is controversial. We note that in several previous studies the outermost H I spiral feature (that we identify as the Outer arm) in Figure 5 has been identified as the Perseus arm (Nakanishi & Sofue 2003; Levine et al. 2006a; Reid et al. 2016a). We, however, identify the relatively diffuse H I ridges running along the inside of the model Perseus arm as the Perseus arm trace. The trace is well-defined between $l \approx 200^\circ$ and 240° , while, between $l \approx 240^\circ$ and 300° , there appears to be two parallel ridges that can correspond to the Perseus arm trace (see also § 3.3). And at its ends ($l \approx 300^\circ\text{--}330^\circ$), the H I arm appears to bifurcate. As we see in Figures 4 and 5, there are HMSFRs around $l = 230\text{--}240^\circ$ and many CO clouds between $l \approx 205^\circ$ and 270° (Vázquez et al. 2008) along our Perseus arm trace, which supports its identity as a spiral arm trace. We can make the model arm to match the H I feature better by increasing ϕ_0 slightly, i.e., $\phi_0 = 117^\circ$ instead of 108° . Levine et al. (2006a) instead fit this segment by a new logarithmic spiral arm of large (25°) pitch angle, while Nakanishi & Sofue (2016) identified it as an extension of the Local arm. McClure-Griffiths et al. (2004), however, identified the ridge between $l = 253^\circ$ and 321° as a separate arm (the ‘‘Distant Arm’’) that can be smoothly connected to the Outer arm by a small (9°) pitch angle. It is worth to note that there are essentially no WISE H II regions at $l \gtrsim 270^\circ$ associated with the H I structure, but only WISE H III regions with measured velocities are shown and therefore the lack of H I regions may be due to less sensitive line surveys of the Southern Galaxy (Brown et al. 2017).

(3) Outer arm

The Outer arm appears as the most prominent H I feature in the northern Galaxy. The segment between $(20^\circ, 8.3 \text{ kpc})$ and $(80^\circ, 13 \text{ kpc})$ is the brightest feature and has been well known (Henderson et al. 1982; Nakanishi & Sofue 2003). But it is systematically shifted outwards from the model spiral arm by $\lesssim 2 \text{ kpc}$, which could be due to non-circular motions associated with streaming along the spiral arm. Between $l = 80^\circ$ and 110° , the arm appears to split into two segments, and at larger l ($110^\circ\text{--}150^\circ$) the structure becomes complex with ridges blending each other. Du et al. (2016) detected CO clouds in this area ($l = 100^\circ\text{--}150^\circ$) and investigated the associated H I structure.

In the southern Galaxy, we identify the outermost, narrow and bright coherent feature between $l = 210^\circ$ and 300° as the Outer arm, which appears as a smooth coherent structure running closely parallel to the model Outer arm. The reason that we associate this structure to the Outer arm and not to the Perseus arm is mainly because there is another distinct arm structure that can be assigned to the Perseus arm as we discuss above. Early H I studies also detected the bright ridges of this structure and identified them as an outer spiral arm beyond the Perseus arm (Kerr 1969; Davies 1972) (Figure 3). In the face-on map, however, there is a large positional jump in the Outer arm trace from the northern to the southern Galaxy across the gap around $l = 180^\circ$ (Figure 5), which led people to identify the bright portion between $l = 210^\circ$ and 260° as the Perseus arm in some previous studies (Nakanishi & Sofue 2003; Levine et al. 2006a). We will address this issue in the next section, but basically there is no jump in (l, v_{LSR}) space, and the jump in the face-on map was generated in transforming v_{LSR} to the Galactocentric distance. On the other hand, the bright portion is relatively straight and is systematically shifted inwards from the logarithmic spiral by $\lesssim 2 \text{ kpc}$. Efremov (2011) pointed out that its morphology is similar to the so-called ‘‘kneed’’ spiral arms in external galaxies. But it could be also due to streaming motions along the spiral arm. Vázquez et al. (2008) detected CO clouds associated with the H I ridge between $l = 190^\circ$ and 255° , and pointed out that their distribution and the H I structure are well

matched to the Outer arm in the four-arm spiral model. At its ends, between $l = 285^\circ$ and 300° , the Outer arm also appears to bifurcate.

(4) Sct-Cen arm

The outer Sct-Cen arm appears as a distinct, $\gtrsim 20$ kpc-long HI arc structure in the outermost northern Galaxy in our face on map. The bright segment between $(15^\circ, 12 \text{ kpc})$ and $(70^\circ, 16 \text{ kpc})$ had been identified in early HI studies (Kerr 1969; Weaver 1974) and was rediscovered recently by Dame & Thaddeus (2011). There is a prominent, ~ 4 kpc-long HI ridge between $(38^\circ, 13 \text{ kpc})$ and $(46^\circ, 12 \text{ kpc})$ with many HII regions, which appears to be an interarm structure (see the Appendix). At $l \sim 70^\circ$, the arm structure becomes faint and bends inwards, and at $l \sim 110^\circ$, it appears to blend with other arc structures. Sun et al. (2015) claimed the ‘flared’ feature between $l = 110^\circ$ and 150° as the continuation of the Sct-Cen arm based on their detection of CO clouds.

In the southern Galaxy, there is strong HI emission along the Sct-Cen arm at $l \approx 320^\circ\text{--}345^\circ$ just outside the solar circle (Figure 4). As we mentioned in § 3.1, most of this emission is from the local HI gas in the solar neighborhood with slightly positive v_{LSR} . But we find that, if we generate a surface density map of HI gas near the Galactic plane, e.g., within $|z| \lesssim 0.5 \text{ kpc}$ from the $b = 0^\circ$ plane, we can see an HI feature that corresponds to the Sct-Cen arm.

3.3. The Perseus and Outer Arm Issue

As mentioned in section 3.2, there is considerable confusion in the extension of the Perseus and Outer arms in the southern Galaxy ($l = 180^\circ\text{--}360^\circ$). A major issue is the identification of the outermost, bright HI ridge between $l = 210^\circ$ and 280° : *Is it an extension of the Outer arm or the Perseus arm?* To summarize, early HI studies (e.g., Kerr 1969; Davies 1972) identified it as an outer spiral arm beyond the Perseus arm. We also identified it as an Outer arm extension because there is another arm feature that can be assigned to the Perseus arm. In contrast, several previous studies identified it as an extension of the Perseus arm that can be connected smoothly across $l = 180^\circ$ with a large ($16^\circ\text{--}24^\circ$) pitch angle (Nakanishi & Sofue 2003; Levine et al. 2006a; Reid et al. 2016a).

The confusion is partly due to the difficulty in tracing the spiral structure near $l = 180^\circ$ in the face-on map where one cannot obtain reliable kinematic distances. So it is helpful to look at an (l, v_{LSR}) map. Figure 7 is an (l, v_{LSR}) map of dense HI concentrations in the 2nd ($l = 90^\circ\text{--}180^\circ$) and 3rd ($l = 180^\circ\text{--}270^\circ$) Galactic quadrants (hereafter Q2 and Q3, respectively) produced by integrating $T_b(l, b, v_{\text{LSR}})$ in § 2 from $b = -5^\circ$ to $+5^\circ$ (see Appendix for other maps integrated over a wider latitude range). The ridges that we associate with the Perseus and Outer arms are marked in green and cyan colors, respectively (see Figure 5 for their locations in real space). Figure 7 clearly shows that the Perseus and Outer arm ridges are both prominent in Q3, e.g., the Perseus arm ridge between $(l, v_{\text{LSR}}) \approx (190^\circ, 20 \text{ km s}^{-1})$ and $(240^\circ, 70 \text{ km s}^{-1})$ and the Outer arm ridge between $(l, v_{\text{LSR}}) \approx (190^\circ, 20 \text{ km s}^{-1})$ and $(260^\circ, 110 \text{ km s}^{-1})$. At larger l , each of them appears to split into two and the structure becomes complicated. The CO clouds and HII regions along the two ridges support the nature of these ridges as spiral arms, and the location of the Perseus-arm HMSFRs with accurate distances (Reid et al. 2016a) around $l = 230^\circ\text{--}240^\circ$ further supports their identity as the Perseus and Outer arm ridges.

Connecting the Perseus and Outer arm ridges in Q3 to those in Q2 across $l = 180^\circ$ is not straightforward. First, the two ridges merge with each other at $l \lesssim 200^\circ$. Indeed, between $l = 190^\circ$ and 180° , all HI features merge into one single ridge because of small $|dv_{\text{LSR}}/dr|$. Then in Q2, the HI spiral structure is complicated. We have traced prominent HI ridges to yield a coherent structure and again the strong spiral tracers along these ridges support their spiral arm nature, but individual segments show considerable deviations from a smooth pattern. The positional jump in the Outer arm trace across the gap near $l = 180^\circ$ in the face-on map, therefore, cannot be strong evidence against its identity as a coherent spiral structure. It is also interesting to note that the Outer arm HI ridges are generally faint in Q2 but bright in Q3, which appears to be implausible considering that the Outer arm in Q3 is at a larger Galactic radius. We think that this could be because our face-on map shows dense HI concentrations, while the outer Galactic disk in Q2 is severely warped and flared so that HI gas there is relatively diffuse. Indeed the contrast in HII regions and CO clouds between Q2 and Q3 for the Outer arm is similar.

4. SUMMARY

Characterizing spiral structure in the outer Galaxy using strong spiral tracers is limited, partly because high-resolution radio observations with sufficient sensitivity are not yet available but also because of the sparsity of those sources. It had been suggested that the intensity maxima of HI 21-cm emission can trace spiral structure, but this has not been explored with the sensitive all-sky LAB data. Here we verify that the face-on map of dense HI concentrations obtained by projecting HI 21-cm line peak intensities is indeed a useful and efficient way to trace spiral structure in the

outer Galaxy. With the caveat that some arm structures may have been shifted and/or deformed due to non-circular motions, it is still a unique way to see the global spiral structure of the Milky Way far out beyond the solar circle. In the following, we summarize our main results:

(1) Our face-on map (Figure 2) strikingly shows the complex H I spiral structure of the outer Galaxy. The structure is characterized by several prominent long ($\gtrsim 20$ kpc) arcs that might be segments of major spiral arms and numerous ridges either connecting these spiral arm features or branching out from them. We confirm the identity of these H I arc structures as spiral arms by comparing them to the distribution of other more conventional spiral tracers, e.g., H II regions, CO clouds, and HMSFRs. Some interarm features are prominent and have associated H II regions.

(2) The global H I spiral structure in the outer Galaxy is consistent with the four-arm spiral model with some deviations. The Sgr-Car and Sct-Cen H I arms have well-established H I features, and they connect well to their HMSFR counterparts in the inner Galaxy by logarithmic spirals with a pitch angle of $12^\circ.4$. This pitch angle agrees with the global pitch angle of the spiral structure determined in previous studies. For the Perseus arm, there is a faint but distinct H I arm feature that can connect to the HMSFRs by a logarithmic spiral with the same pitch angle. For the Outer arm, there are bright H I arc structures wobbling with respect to the logarithmic spiral arm. The H I spiral features show complex structure near the ends; the Perseus and Outer arms bifurcate, while the Sct-Cen arm bends inwards with negative pitch angle. Such variations of pitch angles along individual arms are similar to what we see in other galaxies.

(3) Our results provide an insight into identifying H I features associated with individual spiral arms. In the southern Galaxy, there have been controversies in the identification of H I arc structures corresponding to the Perseus and Outer arms. Our map clearly shows that there are two distinct H I arc structures that can be identified as those two spiral arms. According to our identification, in the southern Galaxy, the H I Outer arm is much more prominent than the H I Perseus arm which is relatively faint and indistinct.

(4) In the Appendix, we show the locations of spiral arm traces in an (l, v_{LSR}) diagram and compare them to the result of previous studies. Our traces are not very different from those in Reid et al. (2016a) except for the Perseus/Outer arms in the third quadrant; Reid et al. identified the H I ridges at the most positive LSR velocities as the Perseus arm, while we consider that those ridges correspond to the Outer arm and that it is the H I ridges at lower positive LSR velocities corresponding to the Perseus arm. We also provide a catalog of prominent interarm structures in the Appendix.

We thank Bob Benjamin for many valuable comments that helped preparing the manuscript. We also wish to thank Tom Dame, Mark Reid, and the anonymous referee for their comments and suggestions which helped us improve the paper. This work was supported by the National Research Foundation of Korea (NRF) grant funded by the Korea Government (MSIP) (No. 2012R1A4A1028713). The National Radio Astronomy Observatory is a facility of the National Science Foundation operated under cooperative agreement by Associated Universities, Inc. T.V.W. is supported by the NSF through the Grote Reber Fellowship Program administered by Associated Universities, Inc./National Radio Astronomy Observatory, the D.N. Batten Foundation Fellowship from the Jefferson Scholars Foundation, the Mars Foundation Fellowship from the Achievement Rewards for College Scientists Foundation, and the Virginia Space Grant Consortium.

Software: IDL

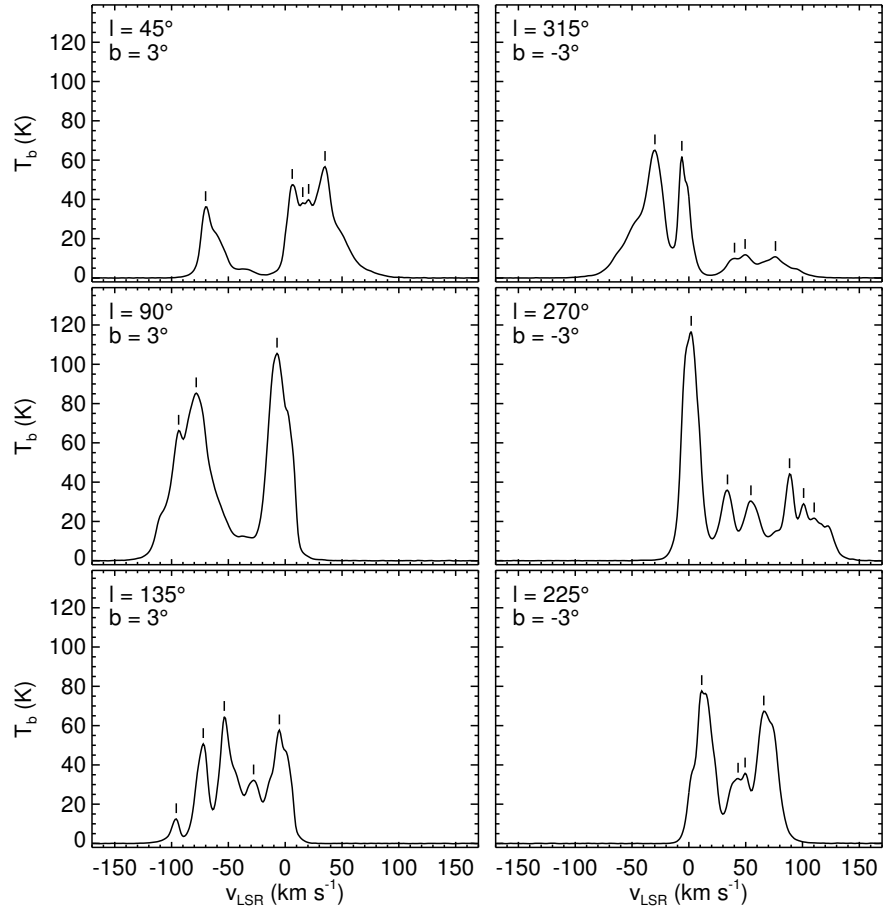


Figure 1. Sample H I spectra of the LAB survey with the local maxima found by the code PEAKFINDER marked (see text for more details). The portions of the profiles corresponding to the emission from the H I gas outside the solar circle for $l = 0^\circ$ – 180° (180° – 360°) are those at $v_{\text{LSR}} < 0$ (> 0).

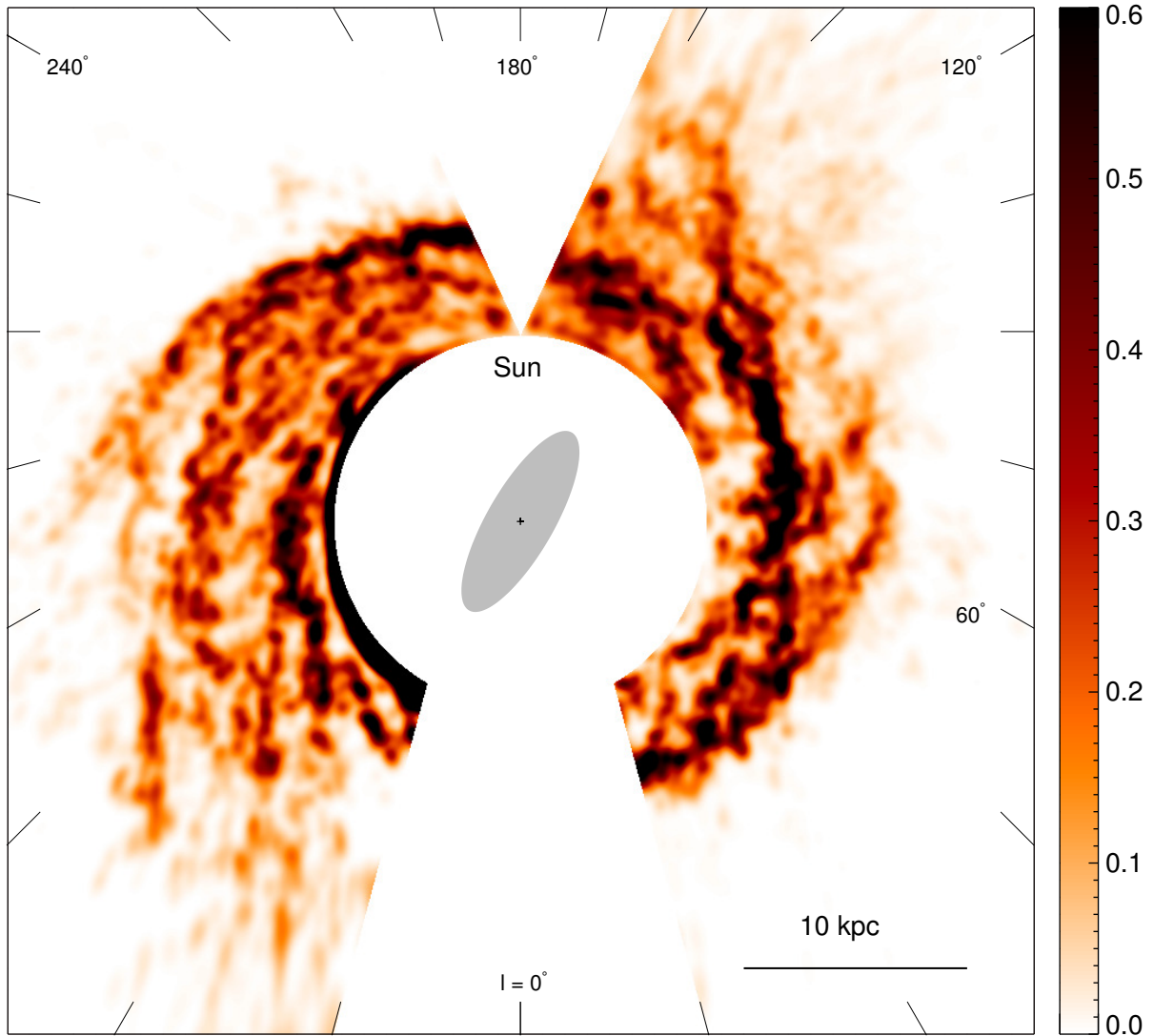


Figure 2. Face-on map of HI concentrations in the Galaxy beyond the solar circle obtained in this paper. The color scale represents the mass surface density (Σ_{HI}) of HI concentrations in units of $M_\odot \text{pc}^{-2}$. It should be noted that the locations of HI concentrations could have been shifted due to non-circular motions (see § 3.1). The wedge-shaped regions and the inner Galaxy are blanked out because no reliable distances to the HI gas can be derived in these areas. Galactic longitudes (l) are marked at intervals of 15° . The filled ellipse near the center indicates the central bar (Wegg et al. 2015).

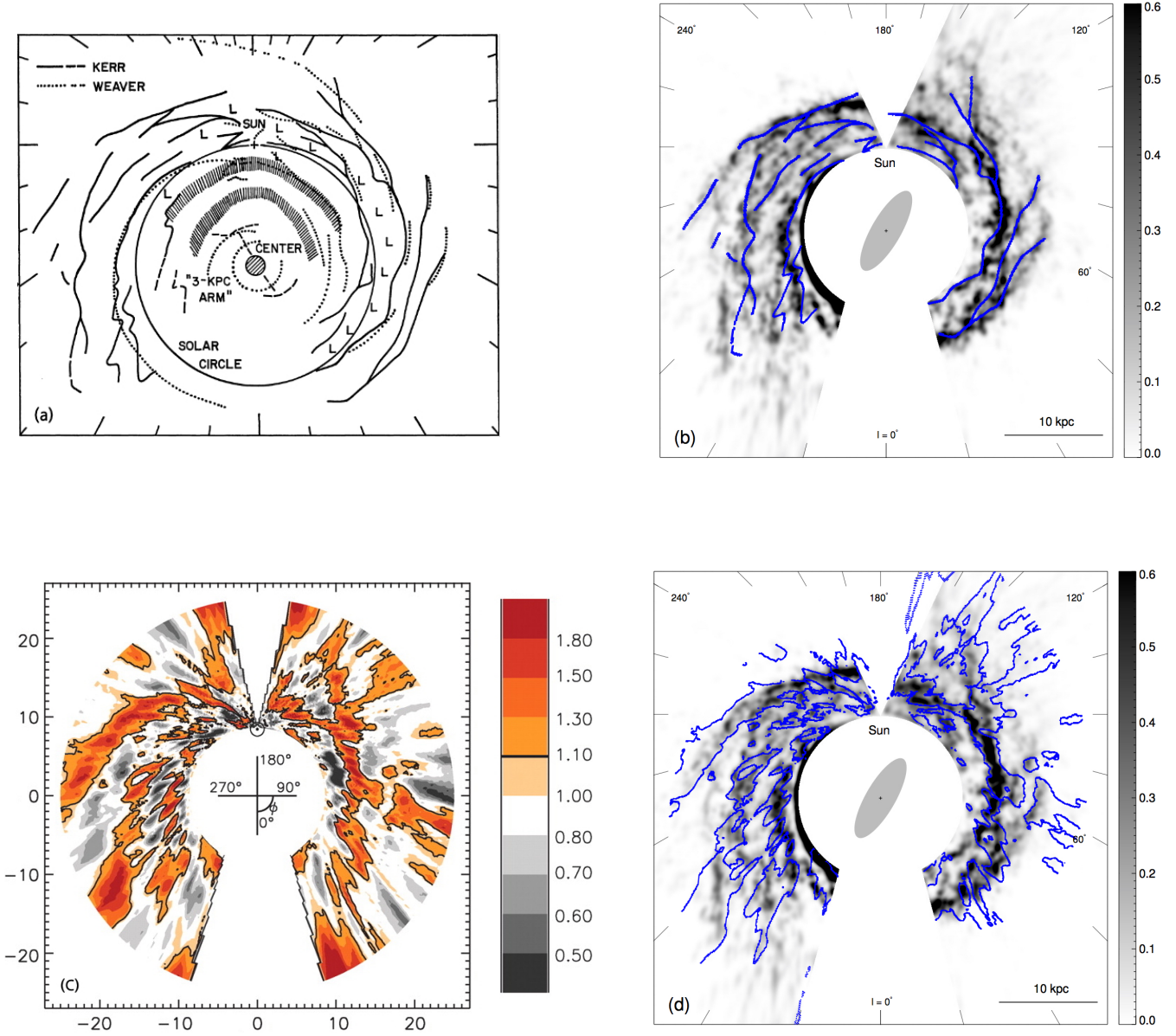


Figure 3. (a) Sketches of H I ridges determined by Kerr (1969) and Weaver (1970) (Figure 1 in Simonson 1970, reproduced with permission © ESO). (b) Same as Figure 2 but with the Kerr's ridges overlaid. Kerr (1969) used the Schmidt rotation curve (Schmidt 1965), and his ridges are reprojected using the flat rotation curve that we adopted in this paper (see § 2). (c) Face-on map of perturbed H I surface density obtained by Levine et al. (2006a) using an unsharp-masking technique (Figure 1 in Levine et al. 2006a, reprinted with permission from AAAS). The color scale represents perturbed H I surface density normalized by a local median value. The x and y scales are in kpc. (d) Same as Figure 2 but with the Levine's contours at 1.10 overlaid. Levine et al. (2006a) used their own rotation curve (see § 2), and their contours are reprojected using the flat rotation curve that we adopted in this paper.

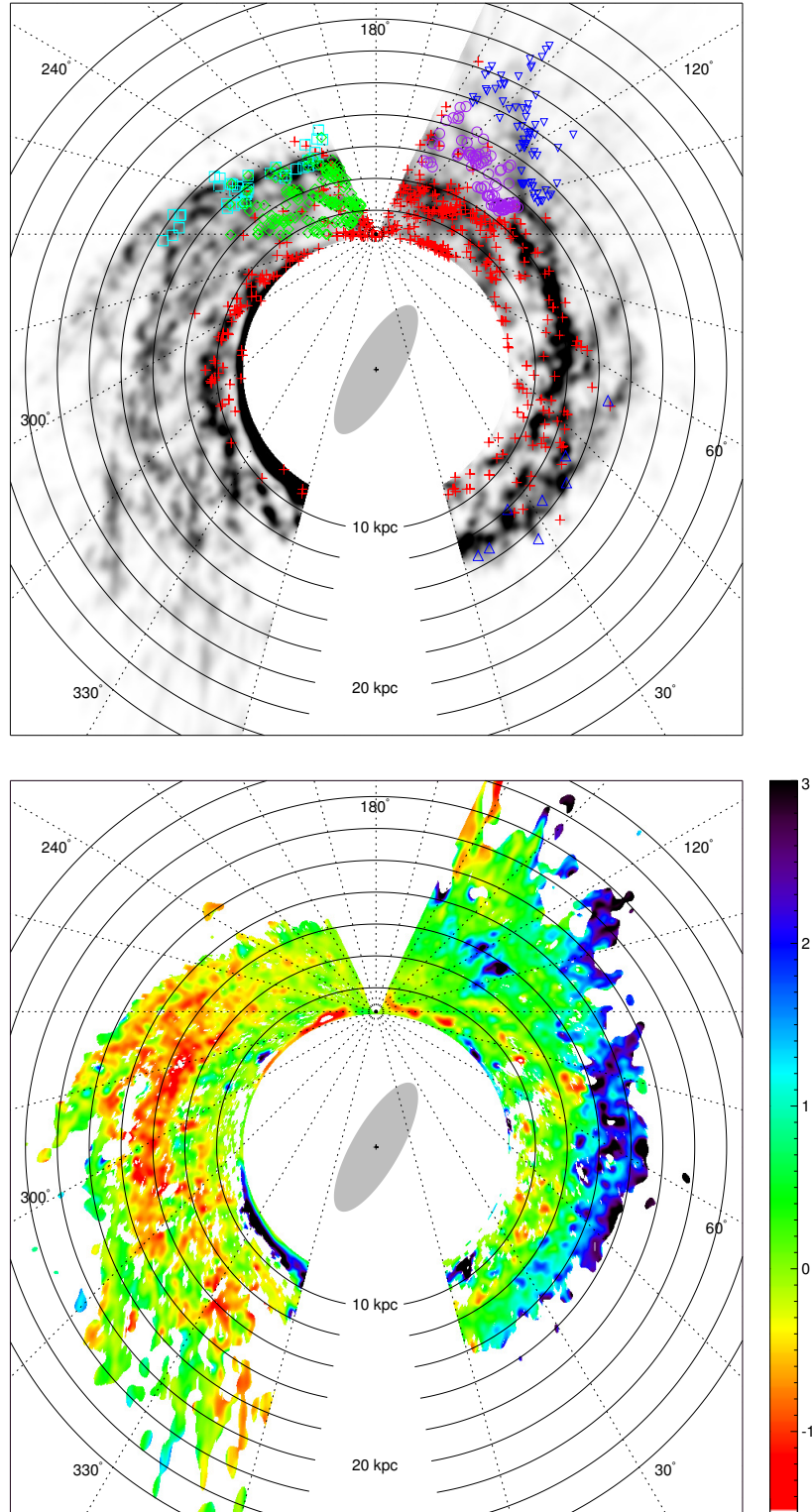


Figure 4. *Top:* H I face-on map with H II regions and CO clouds overlaid: red crosses = *WISE* H II regions (Anderson et al. 2014); other symbols = CO clouds of May et al. (1997) (green diamonds), Vázquez et al. (2008) (cyan squares), Dame & Thaddeus (2011) (blue triangles), Sun et al. (2015) (blue upside-down triangles), and Du et al. (2016) (purple circles). H II regions with multiple velocity components are not drawn, while only CO clouds with masses greater than $5 \times 10^3 M_{\odot}$ are shown for Du et al. (2016). *Bottom:* Mass-weighted mean height, i.e., $\langle z \rangle \equiv \int z \rho(z) dz / \Sigma_{\text{HI}}$, of the H I concentrations with $\Sigma_{\text{HI}} \geq 0.05 M_{\odot} \text{ pc}^{-2}$ in kpc. The color scale varies from -1.5 kpc to $+3$ kpc as in the color bar.

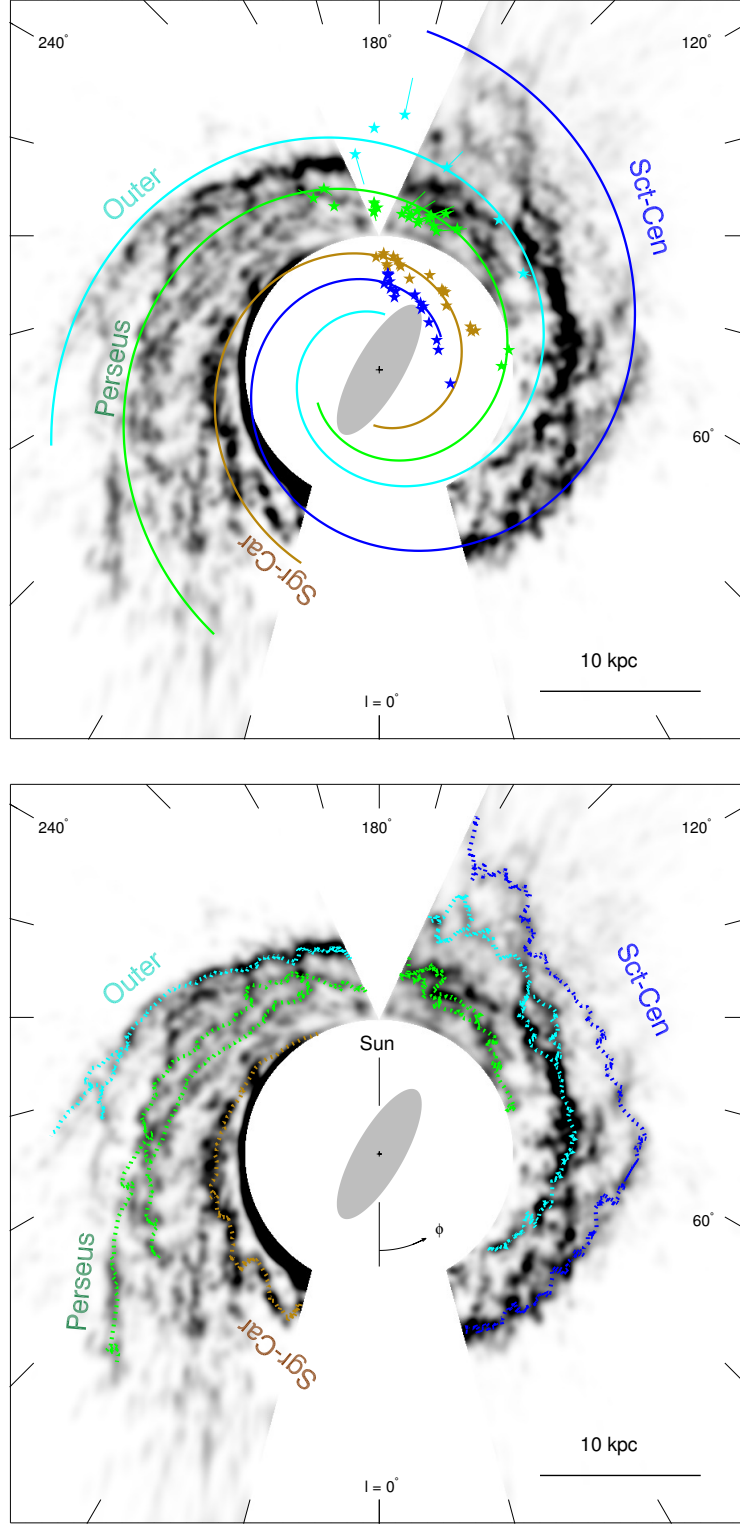


Figure 5. *Top:* H I face-on map with HMSFRs of parallax-determined distances (Reid et al. 2014) overlaid. The HMSFRs are color-coded according to their assigned spiral arms. The attached thin solid lines show the positional shift when their distances are determined from the LSR velocities. The thick solid lines show a four-arm spiral model with a pitch angle of $12^\circ.4$. The Perseus and Outer arms are obtained simply by rotating the other two arms by 180° . See § 3.2 for more details. *Bottom:* H I face-on map with spiral arm traces overlaid. The dotted line represents the H I ridges of the major spiral arms determined in this work (see § 3.2).

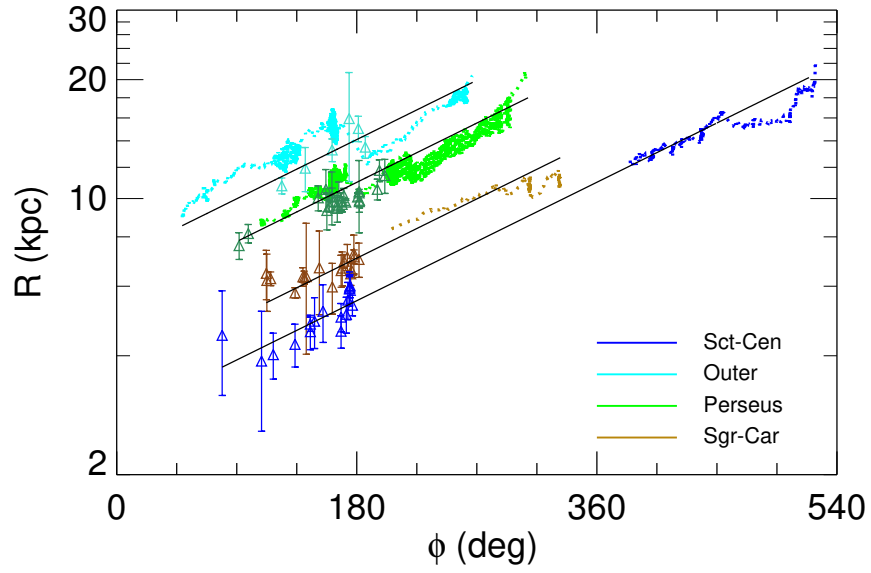


Figure 6. Galactocentric distance (R) versus azimuthal angle (ϕ) of spiral tracers. The dotted lines represent the H I traces in Figure 5, while the empty triangles with error bars denote the locations of HMSFRs (Reid et al. 2014). The black straight lines correspond to the logarithmic spirals of pitch angle $12^\circ.4$. The spirals crossing the Perseus and Outer arms are not the fits but the lines obtained by simply rotating the other two spirals by 180° (see § 3.2).

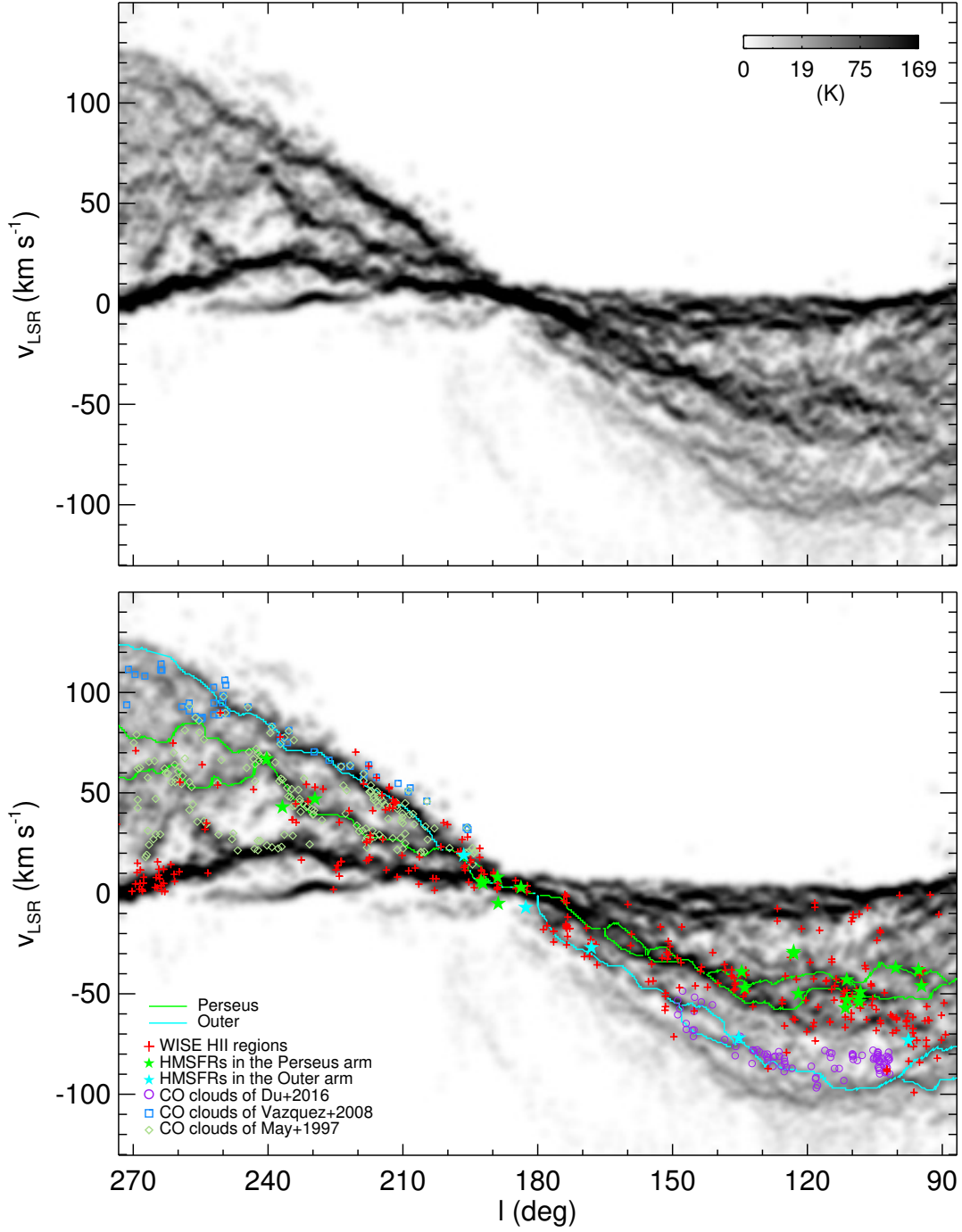


Figure 7. *Top:* H I (l, v_{LSR}) diagram of the Galactic plane obtained by integrating local peaks from $b = -5^\circ$ to $+5^\circ$ (see § 2 and Appendix for more details). The grey scale represents the integrated intensity in K. *Bottom:* Same H I (l, v_{LSR}) diagram but with the ridges that we associate with the Perseus (green) and Outer (cyan) arms traced. The CO clouds and H II regions shown in Figure 4 and the HMSFRs associated with the Perseus and Outer arms (Reid et al. 2016a, see also Figure 5) are also marked .

Table 1. Parameters of Spiral Arms

Arm	Pitch angle (deg)	ϕ_0 (deg)
Sgr-Car	12°:4	223° ± 17°
Perseus	12°:4	108°
Outer	12°:4	43°
Sct-Cen	12°:4 ± 1°:8	288° ± 47°

NOTE—These are the parameters of the spiral arms in Figure 5. The values without error bars represent fixed parameters. The parameters of the Perseus and Outer arms are obtained simply by rotating the other two arms by 180°. See § 3.2 for more details.

APPENDIX

A. DETERMINATION OF SPIRAL ARM TRACES

The spiral arm traces shown in the face-on map in Figure 5 (bottom frame) are obtained in an (l, v_{LSR}) diagram. The diagram was generated from the LAB HI data by integrating the three dimensional cube of local peak intensities $T_{b,\text{max}}(l, b, v_{\text{LSR}})$ along the b axis from $b = -10^\circ$ to $+30^\circ$, which corresponds to 1.8 kpc and 5.8 kpc at a distance of 10 kpc, respectively. This should include all of the warped spiral features. The top frame in Figure A1 shows the resulting (l, v_{LSR}) diagram. We smoothed the map using a Gaussian kernel with FWHM of (3, 3) pixel or (150 pc, 3.06 km s $^{-1}$). Similar maps of the northern Galaxy were produced in earlier studies (Kepner 1970; Weaver 1970; Davies 1972; Verschuur 1973; Weaver 1974), and more recently for the Sct-Cen and Perseus arm features (Reid et al. 2016a). Our (l, v_{LSR}) diagram, however, shows all spiral arm features in an ‘unbiased’ single map.

We identified the ridges delineating the peak positions of integrated intensities using “Discrete Persistent Structures Extractor (DisPerSE)” (Sousbie 2011)⁴ which is open source software for the automatic identification of topological structures such as filaments and voids in 2D and 3D noisy data sets. The software first locates arcs connecting maxima/minima and saddle points, and calculates their ‘persistence’ or the intensity difference between the two end points. Then the arcs with persistence greater than some threshold, e.g., the background intensity of that area, are considered as ‘persistent’ topological features and they are connected to form filaments while the arcs with persistence less than the threshold are eliminated. In our case, after inspecting the persistence versus intensity plot of the arcs in the (l, v_{LSR}) diagram, we adopted a threshold of 1 K to include faint features of the Sct-Cen arm but trimmed the arcs with peak intensities less than 2 K to remove strange and very faint features at high velocities, e.g., below -150 km s $^{-1}$ near $l \sim 130^\circ$. The middle frame in Figure A1 shows the filaments (blue contours) traced by DisPerSE in this way.

The next step is to choose the ridges corresponding to the spiral arms. As explained in the main text, the regularity of the observed HI spiral structure cannot be described by either two- or three-arm models, and we identify the HI ridges corresponding to one of the arms in the four-arm spiral model, i.e., the model with the approximately equally spaced Sgr-Car, Perseus, Outer, and Sct-Cen arms (Georgelin & Georgelin 1976; Wainscoat et al. 1992; Churchwell et al. 2009; Efremov 2011; Vallée 2014, 2015). For the well-established arm features or for the coherent long arc structures, this procedure is rather straightforward. But in the areas with complicated structures or for the features of confusing identity, this procedure is subjective. The most challenging region is the second quadrant from $l = 110^\circ$ to 180° , where the HI ridges split and overlap. Presumably, interarm features as well as non-circular motions due to streaming motions along spiral arms or some large-scale motions with peculiar velocities might be responsible for such complex structures. The bottom image of Figure A1, which shows the mean galactic latitude of HI ridges (\bar{b}), is helpful because \bar{b} should be continuous along an arm and should be close to the latitude of the Galactic midplane. The presence of other conventional spiral tracers, e.g., young stars, star-forming regions, HII regions, and molecular clouds are also helpful (Figure A2 top frame). When there are more than one possible branches, we adopted them both. Figure A2 shows the adopted ridges (solid lines). Adjoining ridges are grouped into segments for convenience, and their start and end locations are listed in Table A1 together with their mean galactic latitudes. There are also bright HI ridges located between the adopted arm ridges, e.g., $(l, v_{\text{LSR}}) = (40^\circ, -54 \text{ km s}^{-1})$ to $(48^\circ, -54 \text{ km s}^{-1})$ between the Outer and Sct-Cen arms, and $(l, v_{\text{LSR}}) = (95^\circ, -67 \text{ km s}^{-1})$ to $(125^\circ, -59 \text{ km s}^{-1})$, and $(l, v_{\text{LSR}}) = (257^\circ, +86 \text{ km s}^{-1})$ to $(282^\circ, +97 \text{ km s}^{-1})$ between the Perseus and Outer arms. We consider them interarm features. Table A2 lists prominent interarm features and Figure A3 shows their locations. Some of them have associated HII regions indicating on-going star formation (see Figure 2).

In the Figure A2 middle and bottom images, we overlay the logarithmic spirals with pitch angles of $12^\circ 4'$ (see main text) and the traces of Reid et al. (2016a), respectively. We will compare our result to that of Reid et al. (2016a) for individual arms below, but in general our traces are not very different from their traces except for the Perseus arm in the third quadrant. Reid et al. (2016a) identified the HI ridges at the most positive velocities as the Perseus arm, but we consider that those ridges correspond to the Outer arm and that it is the HI ridges at lower positive velocities corresponding to the Perseus arm. In the following, we summarize the characteristics of the traces of individual spiral arms:

- (1) Sgr-Car arm

⁴ <http://thierry-sousbie.github.io/DisPerSE/>

The Sgr-Car arm is traced from $l = 282^\circ$ to $l = 347^\circ$, and this is a well known spiral arm feature from early studies (Kerr 1969; Weaver 1970). The segment at $l \lesssim 330^\circ$ is almost identical to that of Reid et al. (2016a) determined from the CO distribution, while the segment at $l \gtrsim 330^\circ$ is seen only in HI. There is a systematic discrepancy between the HI trace and the logarithmic spiral: the trace is located at a velocity higher (lower) than the model at longitudes less than (greater than) 310° . The deviation is less than 10 km s^{-1} mostly, but at $l \lesssim 290^\circ$ it becomes as large as 25 km s^{-1} . This deviation, however, does not yield a significant offset in real space (see Figure 5).

(2) Perseus arm

The Perseus arm is traced from $l = 55^\circ$ to $l = 323^\circ$. At several longitude intervals, multiple branches are allocated, e.g., at $l = 89^\circ\text{--}142^\circ$ and $241^\circ\text{--}323^\circ$. The Perseus arm HI features are well known from early HI studies (Kerr 1969; Weaver 1970), although the features are complex and their allocations are still controversial. Our traces in the first and second quadrants are not very different from that of Reid et al. (2016a) while in the third quadrant, our trace is located at $\sim 15\text{--}30 \text{ km s}^{-1}$ lower velocities. The Perseus arm segment of Reid et al. (2016a) in the third quadrant corresponds to the Outer arm in our case. The segments in the third and fourth quadrants were recently reidentified by McClure-Griffiths et al. (2004) as a separate spiral arm, i.e., the ‘Distant’ spiral arm. The pronounced long ridges with CO clouds, HII regions, and HMSFRs supports our identification (see § 3.3). At $l = 181^\circ\text{--}201^\circ$, HI traces of the Perseus and Outer arms overlap each other because of the velocity crowding. Many WISE HII regions are detected along the Perseus arm, but at $l \gtrsim 270^\circ$, essentially none has been detected. Note that WISE HII regions that considered here are those with measured velocities, but the original WISE catalog lists many HII regions with no available velocity information. So, the absence of HII regions should be checked by further observations.

The Perseus arm traces in the first and second quadrants are complex and located at systematically higher negative velocities than the logarithmic spiral arm model. It has long been known that the Perseus arm in the second quadrant shows non-circular motion of typically $\sim 10\text{--}15 \text{ km s}^{-1}$ (e.g., Miller 1968; Humphreys 1976; Xu et al. 2006; Russeil et al. 2007; Reid et al. 2014). Some of the Reid et al.’s HMSFRs at $l = 100^\circ\text{--}135^\circ$ show larger peculiar velocities ($\gtrsim 20 \text{ km s}^{-1}$). The lower branch at $l = 241^\circ\text{--}323^\circ$ also has a large ($\lesssim 30 \text{ km s}^{-1}$) velocity departure.

(3) Outer arm

The Outer arm is traced from $l = 26^\circ$ to $l = 290^\circ$. At some longitude intervals, multiple branches are allocated, e.g., at $l = 74^\circ\text{--}100^\circ$ and $137^\circ\text{--}149^\circ$. The Outer arm HI ridges had been also identified in early HI studies (Kerr 1969; Weaver 1970; Davies 1972). On the other hand, Reid et al. (2016a) identified these segments as the Perseus arm. As we mention above, however, we identify these segments as being part of the Outer arm since there is a separate, well-defined, segment corresponding to the Perseus arm (see § 3.3). Almost a continuous distribution of CO clouds along the HI ridges has been detected in $l = 100^\circ\text{--}150^\circ$ (Du et al. 2016). Between $l = 100^\circ$ and 120° , there are also CO clouds not associated with HI ridges at somewhat lower ($\sim 20 \text{ km s}^{-1}$) negative velocities. There are many HII regions along the arm at $l \lesssim 100^\circ$ and also along the bright HI ridges beyond.

The HI trace of the Outer arm is not well fit by a logarithmic spiral. There is a systematic offset between the arm traces and any logarithmic arm model: the HI trace has a higher negative velocity than the model in the first and second quadrants while it has a lower positive velocity than the model in the third and fourth quadrants. For our logarithmic spiral model described in the main text, the deviation in the third and fourth quadrants is $\lesssim 20 \text{ km s}^{-1}$, while it is considerably larger ($\lesssim 30 \text{ km s}^{-1}$) in the first and second quadrants.

(4) Sct-Cen arm

The Sct-Cen arm is traced from $l = 6^\circ$ to $l = 184^\circ$. The bright segment between $l = 6^\circ$ and 80° had been identified in early HI studies (Kerr 1969; Weaver 1970, 1974). Our trace agrees with that of Reid et al. (2016a) except at $l = 66^\circ\text{--}120^\circ$ where ours is located at slightly ($\lesssim 10 \text{ km s}^{-1}$) lower negative velocities. Our trace also extends further, i.e., to $l = 184^\circ$ compared to $l = 165^\circ$ of Reid et al. (2016a). CO clouds associated with the segments at $l = 10^\circ\text{--}70^\circ$ and $l = 100^\circ$ and 150° have been detected (Dame & Thaddeus 2011; Sun et al. 2015). There are several HII regions along the former segment.

The linear HI segment at $l \lesssim 66^\circ$ (Sct-Cen_s1) is fit very well by a logarithmic spiral, while at $l = 66\text{--}130^\circ$, the trace significantly ($\lesssim 20 \text{ km s}^{-1}$) deviates from the logarithmic spiral. There is a faint HI feature that can be matched to the logarithmic spiral arm in this longitude range, but its \bar{b} increases continuously beyond $l = 90^\circ$ and therefore is not likely a main spiral feature. (The warping of the Galactic midplane peaks at $l \sim 90^\circ$ and decreases as we move away along azimuth (Levine et al. 2006b).) The segment at $l = 165^\circ\text{--}184^\circ$ (Sct-Cen_s4) is well defined, but it is located at considerably higher negative velocities than the model. In the 4th quadrant, relevant HI features may be there but it

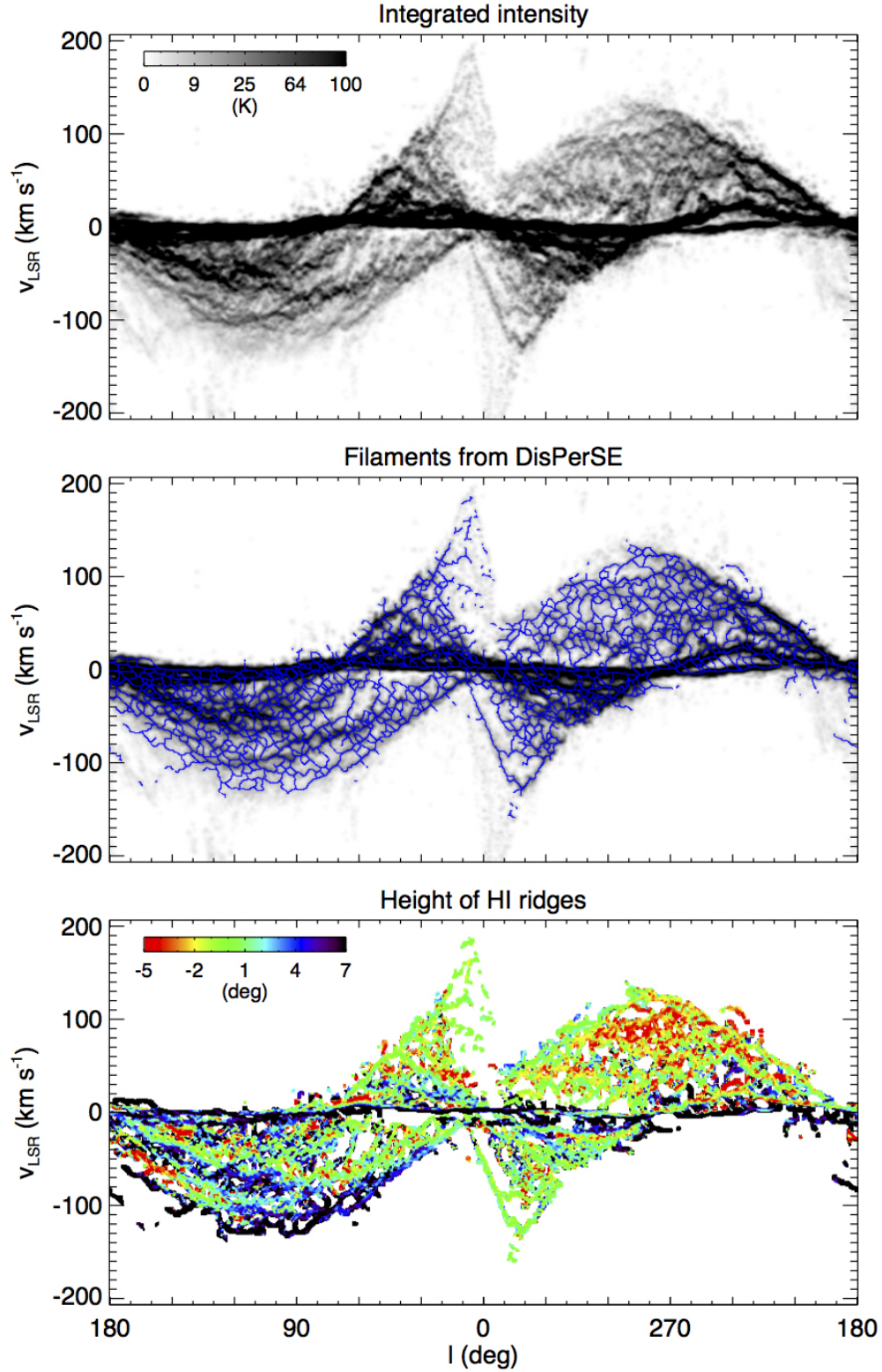


Figure A1. *Top:* H I (l, v_{LSR}) diagram of the Galactic plane obtained by integrating local peaks from $b = -10^\circ$ to $+30^\circ$. The grey scale represents the integrated intensity in K. *Middle:* Filaments found by the software DisPerSE overlaid on the (l, v_{LSR}) diagram. *Bottom:* Intensity-weighted mean height (degrees) of H I ridges along the DisPerSE filaments.

is not clearly seen in the (l, v_{LSR}) diagram shown in the paper due to the contamination by the strong emission from the local H I gas in the solar neighborhood.

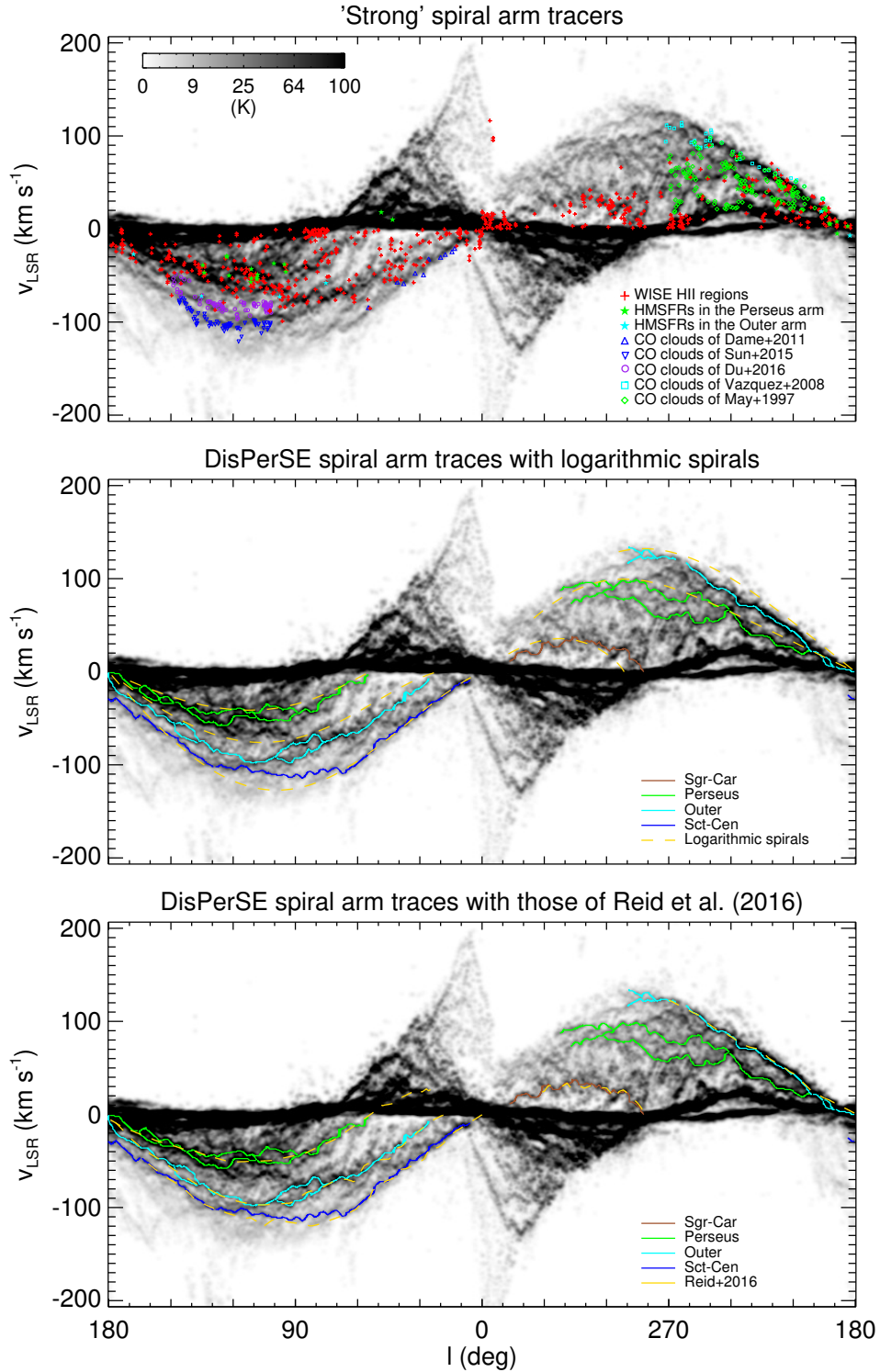


Figure A2. *Top:* Same HI (l, v_{LSR}) diagram as Figure A1 with other conventional spiral arm tracers marked for the outer Galaxy. The tracers are the same as shown in Figures 4–5. The velocities of the HMSFRs are from Table 1 of Reid et al. (2014). *Middle:* The ridges selected as spiral arm traces (zigzagging solid lines) are overlaid on the (l, v_{LSR}) diagram. The dashed yellow lines represent logarithmic spiral arms of pitch angle $12^\circ 4'$ obtained in the main text (Figure 5). *Bottom:* Comparison of our spiral arm traces to those of Reid et al. (2016a). Note that the HI ridges assigned to the Outer arm in the third quadrant were assigned to the Perseus arm by Reid et al. (2016a).

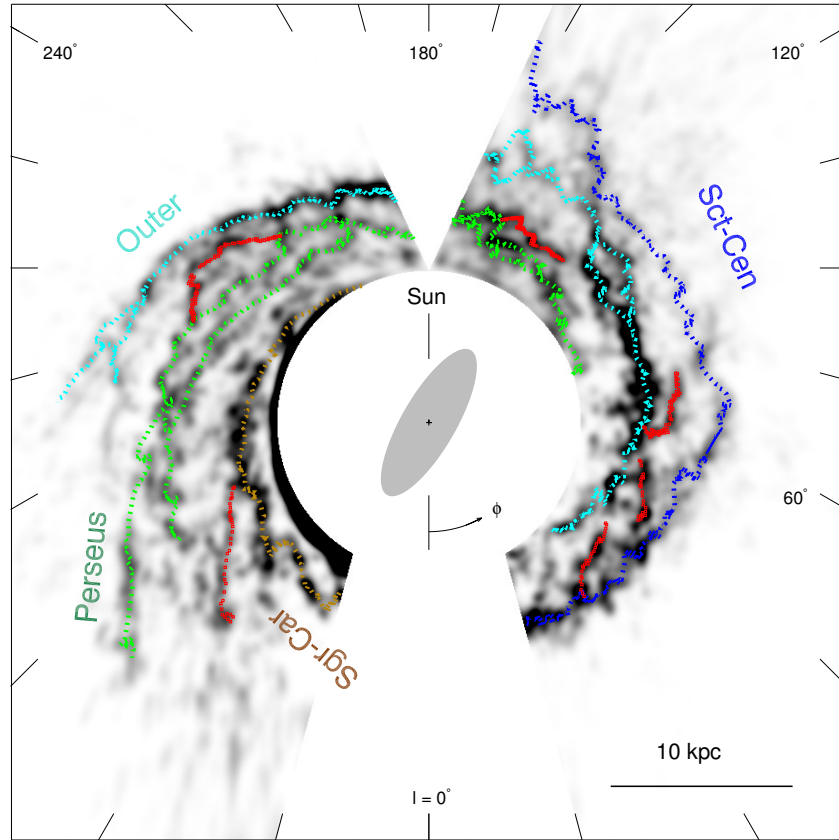
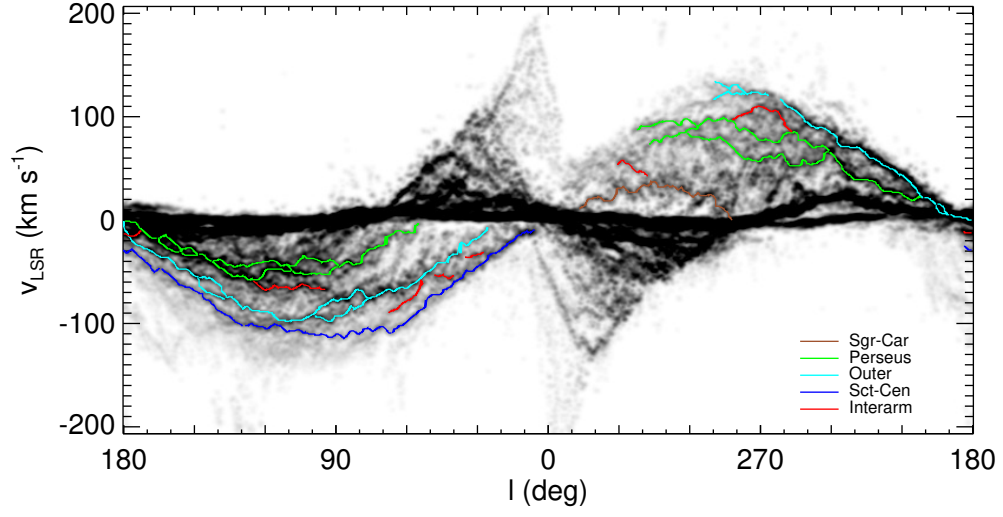


Figure A3. The locations of the prominent interarm features in the (l, v_{LSR}) diagram (top frame) and in the HI face-on map (bottom frame). The grey-scale face-on map is the same as shown in Figure 5 but with the traces of the interarm features marked by red lines.

Table A1. Segments of Spiral Arm Traces

#	Name	Start Location		End Location		Mean \bar{b} ($^{\circ}$)
		ℓ ($^{\circ}$)	v_{LSR} (km s^{-1})	ℓ ($^{\circ}$)	v_{LSR} (km s^{-1})	
1	Srg-Car_s1	282.0	+0.0	346.5	+11.3	-0.4 (1.9)
2	Perseus_s1	55.0	-4.1	88.5	-45.4	+0.6 (1.7)
3	Perseus_s2_1	89.0	-45.4	108.5	-49.5	+0.4 (1.2)
4	Perseus_s2_2	89.0	-44.3	111.0	-42.3	+1.1 (2.2)
5	Perseus_s3_1	109.0	-49.5	142.5	-40.2	+1.7 (1.8)
6	Perseus_s3_2	108.5	-48.4	142.0	-40.2	-0.2 (1.7)
7	Perseus_s4	143.0	-40.2	148.0	-33.0	+0.7 (1.1)
8	Perseus_s5_1	148.5	-34.0	155.5	-32.0	+2.1 (0.7)
9	Perseus_s5_2	148.5	-33.0	156.0	-27.8	-0.4 (0.9)
10	Perseus_s6_1	156.5	-30.9	165.5	-17.5	+1.5 (1.4)
11	Perseus_s6_2	156.0	-30.9	164.5	-17.5	+0.1 (1.4)
12	Perseus_s7	166.0	-17.5	179.5	-1.0	+3.0 (1.3)
13	Perseus_s8	180.5	+0.0	189.5	+5.2	+1.8 (1.2)
14	Perseus_s9_1	190.5	+6.2	195.0	+15.5	+2.8 (5.3)
15	Perseus_s9_2	190.0	+5.2	195.5	+11.3	+0.6 (2.7)
16	Perseus_s10	195.5	+15.5	200.5	+21.6	-0.5 (0.6)
17	Perseus_s11	202.0	+21.6	240.5	+64.9	-0.5 (1.3)
18	Perseus_s12_1	241.0	+67.0	301.5	+85.5	-2.1 (1.3)
19	Perseus_s12_2	241.0	+66.0	301.0	+83.5	-1.9 (1.4)
20	Perseus_s13_1	301.5	+84.5	317.0	+73.2	-2.3 (1.1)
21	Perseus_s13_2	297.0	+89.7	322.5	+87.6	-0.9 (1.1)
22	Outer_s1	25.5	-7.2	73.0	-74.2	+0.3 (1.1)
23	Outer_s2_1	73.5	-74.2	100.0	-91.7	+2.3 (2.3)
24	Outer_s2_2	76.0	-76.3	99.0	-92.8	+3.0 (1.3)
25	Outer_s3	100.5	-92.8	136.0	-75.2	+2.0 (0.8)
26	Outer_s4_1	136.5	-75.2	148.0	-55.7	+2.4 (1.9)
27	Outer_s4_2	137.0	-76.3	148.5	-56.7	+0.9 (0.7)
28	Outer_s5	148.5	-55.7	180.0	-6.2	+2.1 (3.2)
29	Outer_s6	180.5	+0.0	189.5	+5.2	+1.8 (1.2)
30	Outer_s7_1	190.5	+6.2	195.0	+15.5	+2.8 (5.3)
31	Outer_s7_2	190.0	+5.2	195.5	+11.3	+0.6 (2.7)
32	Outer_s8	195.5	+15.5	200.5	+21.6	-0.5 (0.6)
33	Outer_s9	201.0	+21.6	276.0	+121.6	-1.6 (1.2)
34	Outer_s10_1	276.5	+121.6	290.0	+116.5	-1.8 (0.7)
35	Outer_s10_2	276.0	+121.6	289.5	+134.0	-1.3 (1.1)
36	Sct-Cen_s1	6.0	-10.3	66.0	-109.2	+3.2 (1.6)
37	Sct-Cen_s2	66.5	-109.2	128.5	-102.0	+4.7 (2.2)
38	Sct-Cen_s3	129.5	-102.0	164.0	-47.4	-1.5 (2.4)
39	Sct-Cen_s4	165.0	-47.4	183.5	-25.8	-2.1 (4.2)

NOTE— This table lists the segments assigned to the spiral arms where Name=name of arm segment, Start and End locations = (l, v_{LSR}) values of the start and end locations of the segments, and Mean \bar{b} = mean latitude of the segment with standard deviation in parenthesis. For multiple branches, additional numbers are attached to the name, i.e., s2_1 and s2_2, etc.

Table A2. Traces of Prominent Interarm Features

#	Name	Start Location		End Location		Mean \bar{b} ($^{\circ}$)	Arm?
		ℓ ($^{\circ}$)	v_{LSR} (km s^{-1})	ℓ ($^{\circ}$)	v_{LSR} (km s^{-1})		
1	Interarm_s1	25.5	-36.1	35.0	-35.0	+0.8 (1.2)	Sct-Cen
2	Interarm_s2	40.0	-53.6	48.0	-53.6	+1.5 (0.4)	Outer, Sct-Cen
3	Interarm_s3	53.0	-60.8	67.5	-89.7	+3.4 (1.5)	Outer
4	Interarm_s4	94.5	-67.0	125.0	-58.7	+3.1 (1.5)	Perseus
5	Interarm_s5	172.5	-10.3	184.0	-11.3	+5.9 (4.5)	Perseus
6	Interarm_s6	256.5	+85.5	282.0	+96.9	-2.7 (1.2)	Perseus, Outer
7	Interarm_s7	318.0	+42.3	330.5	+53.6	-1.3 (1.1)	Sgr-Car

NOTE—The parameters in columns 3–7 are the same as those in Table A1. The last column lists the spiral arm(s) that might be relevant (see Figure A3).

REFERENCES

- Anderson, L. D., Bania, T. M., Balsler, D. S., et al. 2014, *ApJS*, 212, 1
- Arnal, E. M., Bajaja, E., Larrarte, J. J., Morras, R., & Pöppel, W. G. L. 2000, *A&AS*, 142, 35
- Bajaja, E., Arnal, E. M., Larrarte, J. J., et al. 2005, *A&A*, 440, 767
- Binney, J., & Merrifield, M. 1998, *Galactic astronomy* (Princeton: Princeton University Press)
- Bobylev, V. V., & Bajkova, A. T. 2014, *MNRAS*, 437, 1549
- Brown, C., Jordan, C., Dickey, J. M., et al. 2017, arXiv:1705.08610
- Burton, W. B. 1971, *A&A*, 10, 76
- Burton, W. B. 1974, in *Galactic and Extra-Galactic Radio Astronomy*, ed. Verschuur, G.L., Kellermann, K.I., & Brunt, V. van (Berlin: Springer-Verlag), 82
- Burton, W. B. 1988, in *Galactic and Extra-Galactic Radio Astronomy*, ed. Verschuur & G.L., Kellermann (2nd ed.; Berlin: Springer), 295
- Churchwell, E., Babler, B. L., Meade, M. R., et al. 2009, *PASP*, 121, 213
- Dame, T. M., & Thaddeus, P. 2011, *ApJL*, 734, L24
- Davies, R. D. 1972, *MNRAS*, 160, 381
- Davis, D. R., & Hayes, W. B. 2014, *ApJ*, 790, 87
- Du, X., Xu, Y., Yang, J., et al. 2016, *ApJS*, 224, 7
- Efremov, Y. N. 2011, *Astronomy Reports*, 55, 108
- Erroz-Ferrer, S., Knapen, J. H., Leaman, R., et al. 2015, *MNRAS*, 451, 1004
- Fresneau, A., Vaughan, A. E., & Argyle, R. W. 2005, *AJ*, 130, 2701
- Georgelin, Y. M., & Georgelin, Y. P. 1976, *A&A*, 49, 57
- Hartmann, D., & Burton, W. B. 1997, *Atlas of Galactic Neutral Hydrogen* (Cambridge: Cambridge University Press)
- Henderson, A. P., Jackson, P. D., & Kerr, F. J. 1982, *ApJ*, 263, 116
- Honig, Z. N., & Reid, M. J. 2015, *ApJ*, 800, 53
- Hou, L. G., & Han, J. L. 2014, *A&A*, 569, A125
- Humphreys, R. M. 1976, *ApJ*, 206, 114
- Kalberla, P. M. W., Burton, W. B., Hartmann, D., et al. 2005, *A&A*, 440, 775
- Kepner, M. 1970, *A&A*, 5, 444
- Kerr, F. J. 1969, *ARA&A*, 7, 39
- Kim, Y., & Kim, W.-T. 2014, *MNRAS*, 440, 208
- Levine, E. S., Blitz, L., & Heiles, C. 2006, *Science*, 312, 1773
- Levine, E. S., Blitz, L., & Heiles, C. 2006, *ApJ*, 643, 881
- May, J., Alvarez, H., & Bronfman, L. 1997, *A&A*, 327, 325
- McClure-Griffiths, N. M., Dickey, J. M., Gaensler, B. M., & Green, A. J. 2004, *ApJL*, 607, L127
- Miller, J. S. 1968, *ApJ*, 151, 473
- Nakanishi, H., & Sofue, Y. 2003, *PASJ*, 55, 191
- Nakanishi, H., & Sofue, Y. 2016, *PASJ*, 68, 5
- Oort, J. H., Kerr, F. J., & Westerhout, G. 1958, *MNRAS*, 118, 379
- Reid, M. J., Menten, K. M., Brunthaler, A., et al. 2014, *ApJ*, 783, 130
- Reid, M. J., Dame, T. M., Menten, K. M., & Brunthaler, A. 2016, *ApJ*, 823, 77
- Reid, M. J., & Dame, T. M. 2016, *ApJ*, 832, 159
- Russeil, D., Adami, C., & Georgelin, Y. M. 2007, *A&A*, 470, 161
- Savchenko, S. S., & Reshetnikov, V. P. 2013, *MNRAS*, 436, 1074
- Schmidt, M. 1965, in *Stars and Stellar Systems vol. V. Galactic Structure*, ed. A. Blaauw & M. Schmidt (Chicago), 513
- Simonson, S. C., III 1970, *A&A*, 9, 163
- Sousbie, T. 2011, *MNRAS*, 414, 350
- Sun, Y., Xu, Y., Yang, J., et al. 2015, *ApJL*, 798, L27
- Vallée, J. P. 2014, *AJ*, 148, 5
- Vallée, J. P. 2015, *MNRAS*, 450, 4277
- van de Hulst, H. C., Muller, C. A., & Oort, J. H. 1954, *BAN*, 12, 117
- Vázquez, R. A., May, J., Carraro, G., et al. 2008, *ApJ*, 672, 930
- Verschuur, G. L. 1973, *A&A*, 22, 139
- Wainscoat, R. J., Cohen, M., Volk, K., Walker, H. J., & Schwartz, D. E. 1992, *ApJS*, 83, 111
- Weaver, W. B. 1970, *AJ*, 75, 938
- Weaver, H. 1974, in *IAU Symp. 60, Galactic Radio Astronomy*, ed. F. J. Kerr & S. C. Simonson (Dordrecht: Reidel), 573
- Wegg, C., Gerhard, O., & Portail, M. 2015, *MNRAS*, 450, 4050
- Westerhout, G. 1957, *BAN*, 13, 201
- Xu, Y., Reid, M. J., Zheng, X. W., & Menten, K. M. 2006, *Science*, 311, 54
- Xu, Y., Reid, M., Dame, T., et al. 2016, *Science Advances*, 2, e1600878
- Zhang, B., Reid, M. J., Menten, K. M., et al. 2013, *ApJ*, 775, 79